Ultramicroscopy 111 (2011) 1101–1110

Contents lists available at ScienceDirect

Ultramicroscopy

journal homepage: www.elsevier.com/locate/ultramic

Limits in detecting an individual dopant atom embedded in a crystal

Anudha Mittal, K. Andre Mkhoyan *

Department of Chemical Engineering and Materials Science, University of Minnesota, Minneapolis, MN 55455, United States

A R T I C L E I N F O

Article history:
Received 5 November 2010
Received in revised form
1 March 2011
Accepted 7 March 2011
Available online 15 March 2011

Keywords:
Annular dark field
Scanning transmission electron microscope
ADF
STEM
Dopant
Imaging
High resolution
Si
Ge
Simulations
Multislice

A B S T R A C T

Annular dark field scanning transmission electron microscope (ADF-STEM) images allow detection of individual dopant atoms located on the surface of or inside a crystal. Contrast between intensities of an atomic column containing a dopant atom and a pure atomic column in ADF-STEM image depends strongly on specimen parameters and microscope conditions. Analysis of multislice-based simulations of ADF-STEM images of crystals doped with one substitutional dopant atom for a wide range of crystal thicknesses, types and locations of dopant atom inside the crystal, and crystals with different atoms reveal some interesting trends and non-intuitive behaviours in visibility of the dopant atom. The results provide practical guidelines to determine the optimal microscope and specimen conditions to detect a dopant atom in experiment, obtain information about the 3-d location of a dopant atom, and recognize cases where detecting a single dopant atom is not possible.

© 2011 Elsevier B.V. All rights reserved.

1. Introduction

Interest in imaging and identifying individual dopant atoms inside crystalline specimens has a long history in electron microscopy. While both conventional transmission electron microscopes (TEMs) and scanning transmission electron microscopes (STEMs) are capable of imaging an individual atom [1,2], detecting an individual dopant atom inside the crystal appears to be easiest using an annular dark field detector in STEM. Here a simple relationship between ADF-STEM image intensity and atomic number of scattering atoms provides direct visualization of abnormalities in high-resolution images of crystalline specimens. With recent advances in lens aberration-correction [3–6] ADF-STEM imaging has become applicable even for crystalline sample with <1 Å spacing between atomic columns [7–9].

Challenges in experimentally identifying individual dopant atoms inside crystals using ADF-STEM images include differentiation between a dopant atom inside the sample and an accidental spattered atom attached on the surface of the sample and reduction of electron-beam-induced damage to the sample to the level that local alterations in the specimen will not limit analysis. Imaging dopant atoms in crystalline specimens is further complicated by sample-sensitive changes in the incident electron beam due to channelling [10–13]. However, despite these challenges, several groups have successfully imaged dopant atoms inside a host: Voyles et al. [14] observed Sb atoms inside Si, Varela et al. [15] studied La-doped $CaTiO_3$, Shibata et al. [16] imaged Y atoms in Al_2O_3, Lupini et al. [17] studied Bi dopant atoms in Si, Sato et al. [18] examined the 3-d positions of Pr dopant atoms inside ZnO crystal, and Okuno et al. [19] visualized Tm dopant atoms inside GaN quantum dot. Yet, the number of cases reported in literature are too few to develop a systematic view on parameters and conditions that govern visibility of individual dopant atom in ADF-STEM images. Understanding the roles of the microscope parameters and specimen conditions are instrumental in designing experiments to detect individual dopant atoms and determine their location as precisely as possible to reconstruct the atomic structure of the doped material.

Some simulation-based studies on the visibility of dopant atoms in ADF-STEM have been reported before [20–22,12,13,17]. Voyles et al. [12] have examined the effect of dopant atom position on visibility for non-corrected probes by using Sb-doped Si crystal and observing a rise and fall in visibility as dopant atom depth increases due to beam channelling. Dwyer and Etheridge [22] reported that different sized probes channel differently in a crystal and thus have different positions of maxima in

* Corresponding author. Tel.: +1 612 625 2059; fax: +1 6126267246.
E-mail address: mkhoyan@umn.edu (K.A. Mkhoyan).

0304-3991/$ - see front matter © 2011 Elsevier B.V. All rights reserved.
doi:10.1016/j.ultramic.2011.03.002

intensity as they propagate along an atomic column, suggesting that a dopant located at certain depths inside a crystal can be detected more easily with a larger probe. Lupini et al. [17] and Xin et al. [13] simulated defocal series of ADF-STEM images of doped crystals and showed changes in the brightness of the doped column, suggesting that defocus of the probe might be used to determine the dopant atom position in the 3rd dimension. Xin et al. [13] also reported that a slight tilt away from a low-order zone-axis might improve the visibility of dopant atoms. While the effects of some experimental conditions on the visibility of dopant atoms have been explored, a systematic study of the effects of different parameters to understand limits in visibility of dopant atoms under different specimen and microscope conditions is not present in literature.

In this paper, we have investigated the limits of ADF-STEM imaging to determine presence and position of individual dopant atoms inside the host crystal by analysing simulated ADF-STEM images. Specimen features, such as thickness and crystallographic orientation of the host material, position of a dopant atom inside a specimen, *Z*-difference between dopant element and host, and probe parameters that affect the visibility of a dopant atom have been examined. This analysis provides a guide for optimization of the conditions for improving detection of a dopant atom and assessment of the conditions under which a dopant atom is not detectable at all in ADF-STEM images.

2. Methods

ADF-STEM images of single-atom-doped Si crystals were simulated using the multislice method [23] and code developed by Kirkland [24]. Silicon was used as a host material because it is commonly doped for electronic applications and is standard for (S)TEM analysis. Other elements in group 14 were used as substitutional dopant atoms because they have the same valence electron configuration as silicon. Strain in the crystal structure due to dopant atom was not included in simulation, but is expected to have very little effect on the visibility of a dopant atom [16]. Specimen thicknesses ranging from 0.5 to 70 nm were examined, covering the regime of nanoparticles and polished wedge samples. Dopant atom positions range from beam entrance surface of the sample to 18 nm deep inside a crystal (see Fig. 1).

Si samples were examined from three different orientations, [1 0 0], [1 1 0], and [1 1 1]. Supercell sizes of the Si specimens used in simulations were 36.65×36.65 Å^2 for [1 0 0] oriented crystal, 28.79×31.22 Å^2 for [1 1 0] and 28.80×32.14 Å^2 for [1 1 1]. A grid with 512×512 pixels was used for 100 keV beams and 1024×1024 for 300 keV. Crystals oriented along [1 0 0], [1 1 0], and [1 1 1] directions were sliced with thicknesses 1.36, 1.92, and 0.7 Å [25], respectively. For generation of ADF-STEM images, the STEM probe was scanned with 8 pixel/Å steps across the sample. In all images, the intensity is normalized to the incident beam intensity, which is the same in all simulations. This normalization allows quantitative comparison between different images. Beam intensity profiles along an atomic column in Si for different crystallographic orientations and other host materials were also simulated to study beam channelling.

Four types of STEM probes were used: (i) 100 keV aberration-corrected probe, $C_{s(3)} = -0.015$ mm, $C_{s(5)} = 10$ mm, $\Delta f = -30$ Å defocus, and $\alpha_{obj} = 25$ mrad objective aperture [26]; (ii) 100 keV non-corrected probe, $C_s = 1.3$ mm, $\Delta f = 850$ Å defocus, and $\alpha_{obj} = 11.4$ mrad objective aperture; (iii) 300 keV aberration-corrected probe, $C_{s(3)} = -0.015$ mm, $C_{s(5)} = 10$ mm, $\Delta f = -5$ Å defocus, and $\alpha_{obj} = 25$ mrad objective aperture; and (iv) 300 keV non-corrected probe, $C_s = 1.3$ mm, $\Delta f = 320$ Å defocus, and $\alpha_{obj} = 11.4$ mrad (see Fig. 2). While the actual parameters for aberration-corrected and non-corrected probes vary for different STEMs and experiments, the general characteristics, such as probe size or convergence angle, are very similar. In the simulations the probe was focused on the specimen entry surface, since it is the optimum condition for the smallest incident probe and for imaging the bulk of the crystal. Electrons scattered between 54 and 200 mrad from the optic axis were collected to form the ADF-STEM images. Effects of chromatic aberration and source size were ignored. Thermal vibrations of the atoms were modelled by averaging 10 different frozen phonon configurations for each ADF-STEM image [21]. The room temperature RMS atomic displacement (or vibration amplitude) of 0.076 Å was used in simulations with Si host [21,27] and 0.08 Å in simulations with Ge host [28]. Analysis of the effect of host Z required study of Sn as host material, in which case Sn was modelled with Si atomic structure and RMS atomic displacement for thermal vibrations to prevent results from being a coupled effect with change in crystal structure.

At high resolution, ADF-STEM images show bright intensities at atomic column positions. The intensity of each column increases with the atomic number of the elements of the column. Hence, a single dopant atom is detected due to difference in intensities of doped and non-doped columns. Visibility, *V*, of a dopant atom is defined here as

$$V = \begin{cases} \frac{I_D - I_H}{I_H} \times 100\% & \text{if } Z_{Dopant} > Z_{Host}, \\ \frac{I_H - I_D}{I_H} \times 100\% & \text{if } Z_{Dopant} < Z_{Host}, \end{cases} \quad (1)$$

where I_D is the intensity of a doped column and I_H is the intensity of a non-doped column in ADF image, Z_{Dopant} and Z_{Host} are the

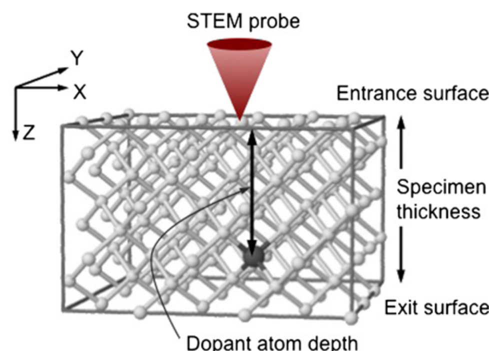

Fig. 1. Schematic representation of doped specimen and STEM probe.

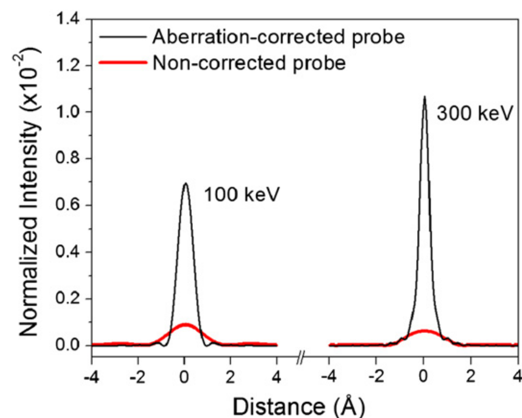

Fig. 2. Four different STEM probes used in these simulations: aberration-corrected and non-corrected probes at 100 and 300 keV.

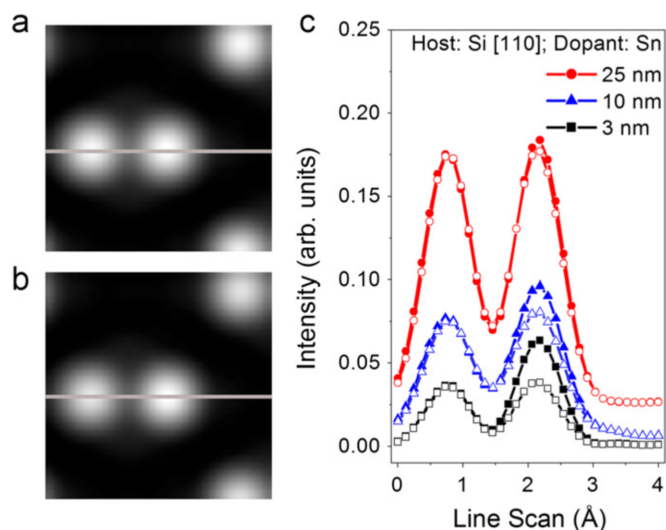

Fig. 3. (a) ADF-STEM image of Si in [1 1 0] orientation. (b) ADF-STEM image of Sn-doped Si in [1 1 0] orientation. (c) Line scans from images in (a) and (b) and similar images of specimens of different thicknesses. Solid markers are line scans from Sn-doped Si and open markers are line scans from pure Si. The line scans show that the nearest neighbour column has the same intensity as an atomic column in a non-doped specimen of same thickness for thin specimens. The 100 keV aberration-corrected probe was used in these simulations.

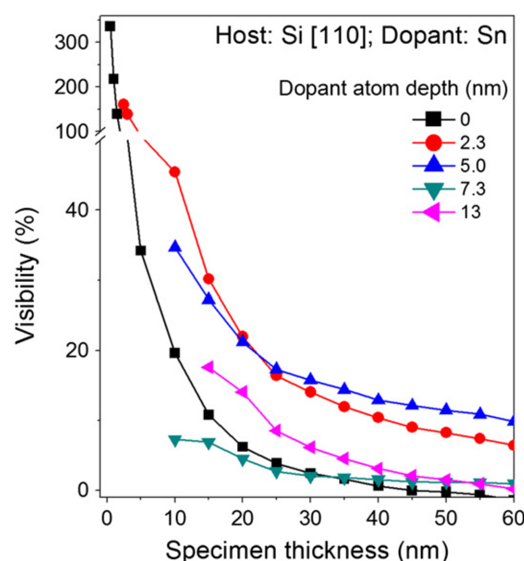

Fig. 4. Visibility of Sn dopant atom in ADF-STEM images as a function of specimen thickness. The host is Si crystal in [1 1 0] orientation. The 100 keV aberration-corrected probe was used in these simulations.

atomic numbers of dopant atom and element of the host crystal, respectively.

The intensity of a non-doped column is taken from the ADF-STEM image of a non-doped host simulated under the exact same conditions as a doped specimen case. In experiment, it is easier to compare intensities of a doped column to neighbouring columns rather than a separate non-doped specimen, and therefore any effect of dopant on neighbouring columns must be understood. We compared the ADF-STEM image intensity of a column adjacent to a doped column to the intensity of a column in a non-doped specimen. ADF-STEM images of Si in [1 1 0] orientation with line scans for specimens of thickness 3, 10, and 25 nm are presented in Fig. 3. These results indicate that in Si in [1 1 0] orientation, in the same dumbbell, the non-doped atomic column has the same intensity as a column in a non-doped Si specimen. We found the same result for adjacent columns also for Si in [1 0 0] orientation. Therefore, I_H in Eq. (1) can be the intensity of the adjacent column in experimental images. However, in thick specimens, typically >25 nm, it is necessary to avoid nearest neighbour columns as reference because a significant amount of beam intensity transfers to the neighbouring columns [29,12,30]. Fractional uncertainty in the value for visibility was estimated by conducting repetitive simulations and propagation of error through the formula for visibility and found to be less than 7% [31].

3. Results

The results of simulations indicate that the visibility of a dopant atom in ADF-STEM images depends strongly on specimen thickness and crystallographic orientation with respect to the incident beam, dopant atom type and position inside the host, the crystal structure and composition of the host material, and on incident beam properties. Here, we discuss each effect separately.

3.1. Effect of specimen thickness

Visibility of an Sn-dopant atom embedded in Si [1 1 0] oriented specimens with thicknesses ranging from 0.5 to 70 nm was examined. Dopant atom depth varies from 0 to 18 nm, but only selected results up to 13 nm depth are shown in Fig. 4 for clarity. Fig. 4 shows that the visibility of a dopant atom decreases drastically with increasing specimen thickness. This is at least partially due to the increase in number of host atoms contributing to the atomic column intensity while there is still only one dopant atom. Visibility decreases monotonically with increasing specimen thickness for all positions of dopant atoms. However, the rate of decrease in visibility varies with dopant atom position. For example, while the visibility of Sn dopant atom on the entrance surface drops from above 200% in 1 nm thick sample to 4% in a 25 nm sample, the visibility of a dopant atom located 5 nm below the entrance surface drops only from 35% in 10 nm thick sample to 10% in 70 nm sample. The rate of decrease in visibility with thickness is slower for dopant atoms that are slightly below the entrance surface. This is due to differences in beam intensity at different depths.

Shibata et al. [16] suggest that the visibility of dopant atom is less dependent on specimen thickness if the specimen is viewed from high-order zone-axes. However, the visibility decreases when crystal is imaged along high-order zone-axis due to higher background intensity in the image [11]. The trade-off requires optimizing conditions for a particular sample. For thin samples, such as nanoparticles, a low-order zone-axis may be the preferred viewing direction because visibility of a substitutional dopant atom is increased due to electron channelling and not destroyed by the high background caused by a large specimen thickness. For dopant atoms embedded in a thick host, imaging along a high-order zone-axis or a slight tilt away from a low-order zone-axis may increase visibility of dopant atoms because visibility drops drastically with increase in specimen thickness when viewed along a low-order zone axis.

3.2. Effect of dopant atom position

It has been reported that the position of a dopant atom along the z-axis affects its visibility [20,29,12,13]. The relationship between dopant atom position and its visibility is studied by calculating the visibility of an Sn dopant atom located at a range of depths from the incident beam's entrance surface in Si [1 1 0] crystal, $d=0$–18 nm, for specimens of different thicknesses.

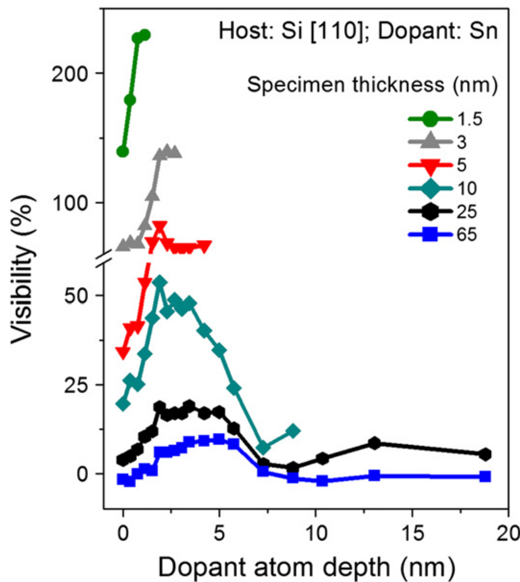

Fig. 5. Dopant atom visibility in ADF-STEM images as a function of dopant atom depth for Sn-doped Si viewed in [1 1 0] orientation. The 100 keV aberration-corrected probe was used in these simulations.

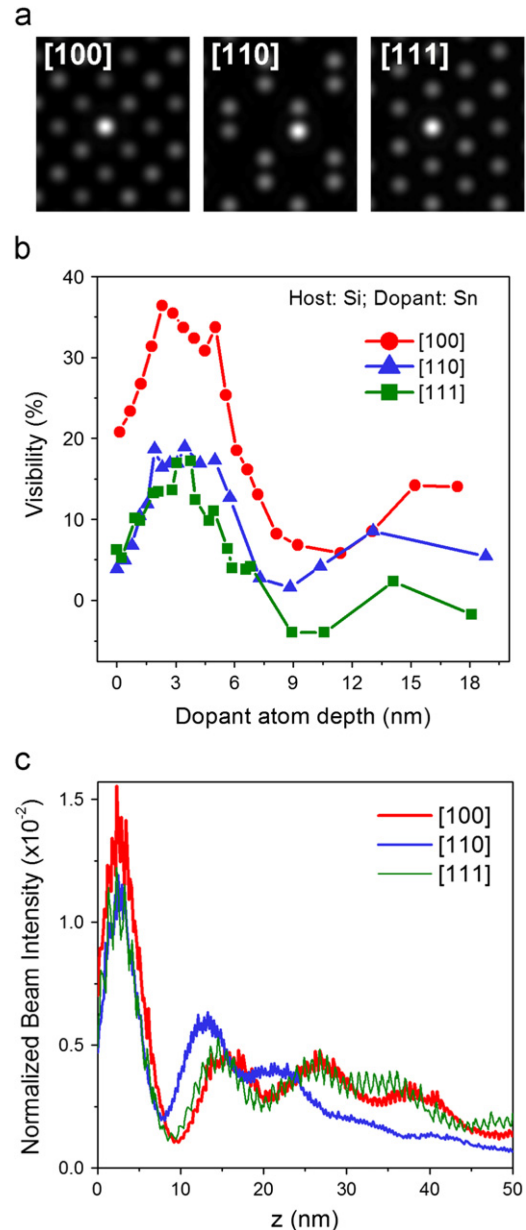

Fig. 6. (a) ADF-STEM images of 3 nm thick Si specimens with single Sn dopant atom located 2.7 nm below the entrance surface viewed along [1 0 0], [1 1 0] and [1 1 1] low-order zone-axes. (b) Visibility of Sn atom in ADF-STEM images as a function of dopant atom depth for these three crystallographic orientations. (c) Incident beam intensity as electrons of the probe, located on the atomic column, propagate along [1 0 0], [1 1 0] and [1 1 1] crystallographic orientations. The 100 keV aberration-corrected probe was used in these simulations.

As can be seen from Fig. 5 the visibility peaks first at approximately d = 2–4 nm and then at around d=13 nm. This non-monotonic behaviour in visibility is due to increase and decrease in intensity of the incident beam along an atomic column, commonly referred to as channelling, causing dopant atoms located at certain positions to scatter more electrons into the ADF detector. Simulated beam intensity profile of an electron-beam propagated in Si [1 1 0] has peaks at 3 and 13 nm, as shown later in Fig. 6(c).

The relationship between visibility and dopant atom depth varies with specimen thickness. The first peak shifts towards a deeper dopant atom as specimen thickness increases. For example, the visibility of dopant Sn peaks around 2 nm depth for a 10 nm thick specimen, whereas it peaks around 4 nm for a 65 nm thick specimen, see Fig. 5.

The non-linear relationship between visibility and depth of dopant atom (see Fig. 5) indicates that comparison of experimental data from recorded ADF-STEM images with simulated results is necessary for gauging the position of the dopant atom. Local slopes in visibility vs. dopant atom depth curve define how precisely can dopant atom location can be determined in that region. Fig. 5 shows that in some ranges for dopant atom positions, visibility changes more than in others. For example, in 25 nm thick [1 1 0] oriented Si, Sn dopant atom has approximately the same visibility if it is 2–5 nm depth range from the entrance surface. Hence, it would not be possible to discern the position of Sn dopant atom within this range. Following this plateau, the visibility drops from 17% to almost 0 within 2–3 nm depth. In this region, careful comparison of the experimental data with simulation may provide a more accurate estimate of dopant atom position. It still may be only possible to narrow the possible dopant atom locations, and not know the exact location because of the region prior to the plateau. Dopant atom at depths 0–2.5 nm also has the same visibility range.

In amorphous hosts the position of dopant atom can be determined within the depth of focus of the STEM probe, which is about 5–10 nm in aberration-corrected probes [32], through defocal series [33,13]. In crystalline hosts this analysis becomes non-intuitive due to probe channelling. It has been observed that in crystalline hosts the intensity of a doped atomic column is more sensitive to the depth of the dopant atom than the defocus and the maximum intensity does not necessarily occur at a defocus equal to dopant atom depth [17]. These complications prevent application of the simple defocal series technique to gauge the depth of a dopant atom in a crystalline host.

In very thin samples the visibility of a dopant atom in ADF-STEM images has a monotonically increasing behaviour as a function of dopant atom depth. In [1 1 0] oriented Si, if the sample is <3 nm thick, the position of the dopant atom can be unambiguously and precisely determined by comparison of experimental data with simulations (see Fig. 5). When a sample is that thin, the visibility of dopant atom is at it maximum when the dopant atom is located at the specimen exit surface, which is consistent with earlier observations by Loane et al. [11], who

report that a Bi adatom on the exit surface of Si is more visible than on the entrance surface.

3.3. Effect of crystal orientation

Crystal orientation is also expected to play an important role in visualizing individual dopant atoms because the beam intensity profile along an atomic column changes with crystal orientation [26]. ADF-STEM images of Sn-doped Si viewed in three different crystallographic orientations: [1 0 0], [1 1 0], and [1 1 1] were simulated and the results are shown in Fig. 6. Visibility of an Sn dopant atom, located at a range of depths, in 25 nm thick Si samples was calculated for each orientation (see Fig. 6(b)). General behaviour of visibility as a function of dopant atom depth is the same for all three orientations, which can be explained by the similarity in beam intensity profiles along these three orientations, see Fig. 6(c). While in all three orientations the first channelling peak is about 3 nm, the position of the second peak varies from 13 nm for [1 1 0] orientation to 16 nm for [1 1 0], the effect of which can be seen in visibility graphs.

The magnitude of visibility is significantly higher in [1 0 0] orientation compared to the other two. This is due to the lower background intensity, I_H, of the non-doped columns in ADF-STEM images in [1 0 0] orientation. We also observed negative visibility of the Sn dopant atom if it is imaged along the [1 1 1] orientation and is located at about 10 nm depth. Thus, testing different crystal orientations for different materials may proves beneficial in detecting dopant atoms. The similarity of the visibility curve for different orientations of the host crystal indicates that concerns with identifying the precise location of single dopant atom from experimental data, discussed in the previous section, is not specific to one unique orientation.

3.4. Effect of type of dopant atom

The difference between atomic number of host and dopant, denoted by ΔZ and formally defined here as

$$\Delta Z = |Z_{Dopant} - Z_{Host}|, \tag{2}$$

causes the difference in ADF image intensity between doped and non-doped columns. It is generally expected that increase in ΔZ would increase visibility of a dopant atom since ADF intensity is directly dependent on atomic number of scattering atom [34–36]. However, it is not obvious how much the visibility would increase per ΔZ. In particular, it is useful to identify the minimum ΔZ that can be detected for given host. To analyse this, we simulated ADF-STEM images of Si ($Z_{Si}=14$) crystal doped with substitutional Sn ($Z_{Sn}=50$), Ge ($Z_{Ge}=32$), and C ($Z_C=6$) dopant atoms, and a vacancy point defect. The position of the point defect and the specimen thickness were varied to understand the effects of ΔZ without coupling with effects of specimen thickness or dopant atom position.

Fig. 7 shows that as ΔZ increases, visibility increases regardless of thickness of the sample or position of the dopant atom, as expected. When 3 nm thick Si oriented along [1 1 0] direction is doped at the entrance surface, the visibility increases 1.7% per atomic number, in which case a minimum $\Delta Z \geq 2$ is required to detect the dopant atom. For a 3 nm thick sample, where dopant atom is located 2.7 nm below the surface at the peak visibility position (see Fig. 5), preferable for experimental study, the visibility increases to about 4% per atomic number. Here, a ΔZ as small as 2 can be detected. For more common wedge polished samples with typical thickness of 25 nm, a surface dopant atom is practically invisible. However, for a dopant atom at most favourable position; 2.7 nm below the surface (see Fig. 5), the visibility of dopant atom in ADF images increases as $0.5\%/\Delta Z$ suggesting that even $\Delta Z = 2$ can be detected. In actual experiment the limit of detectable ΔZ will be dominated by the noise level of the instrument. Once it is identified, the rates indicated here can be used to determine the minimum detectable ΔZ for that STEM.

We also simulated ADF-STEM images of doped Ge [1 1 0] crystals with dopant atom located 0.8 nm below the entrance surface. In one case Ge was doped with Si providing $Z_{Si}-Z_{Ge} = -18$ and in the other case with Sn providing $Z_{Sn}-Z_{Ge} = +18$. Results presented in Fig. 8 show that the dopant atom with $Z_{Dopant} > Z_{Host}$ is almost always more visible than dopant atom with $Z_{Dopant} < Z_{Host}$ even with the same ΔZ.

As was discussed before, the change in visibility depends strongly on specimen thickness and dopant atom position, making it almost impossible to generalize how much it changes with ΔZ, and what is the minimum detectable ΔZ. To illustrate this, Fig. 9 shows the dependence of visibility for each kind of dopant atom and vacancy point defect in ADF-STEM image as a function of sample thickness and position of dopant atom calculated for Si host crystal when it is viewed along [1 1 0] crystallographic direction.

3.5. Effect of host atomic number

The effect of host atomic number in the visibility of a dopant atom is analysed by studying ADF-STEM images of doped Si, $Z_{Si} = 14$, and Ge, $Z_{Ge} = 32$, crystals (both have diamond crystal structure and similar lattice constants, $a_{Si} = 5.430$ Å and

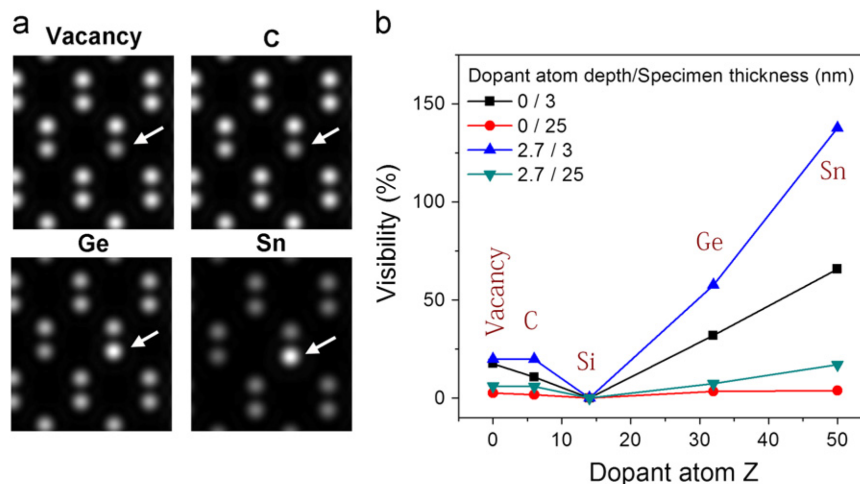

Fig. 7. (a) Simulated ADF-STEM images of 3 nm thick Si crystal in [1 1 0] orientation with single vacancy point defect and C, Ge, and Sn substitutional point defects located 2.7 nm below the entrance surface. The arrow points to the atomic column where dopant atom or vacancy is located. (b) Visibility of each point defect for specimen thickness 3 nm and 25 nm and point defect at the entrance surface and 2.7 nm deep in the crystal. 100 keV aberration-corrected probe was used in these simulations.

$a_{Ge}=5.646$ Å). Si was doped with Ge, and Ge was doped with Sn, $Z_{Sn}=50$, with $\Delta Z=18$ in both cases. This allows us to study the effect of host crystal atomic number without coupling with the effect of ΔZ difference, which is the main source for contrast in ADF-STEM images. Results suggest that the visibility decreases with increase in host atomic number due to increase in intensity of host atomic column, I_H, in ADF image. In Fig. 10 ADF-STEM image intensities of doped and non-doped atomic columns of Si [1 1 0] and Ge [1 1 0] are compared. While differences in image intensity between doped and non-doped specimens can be observed in both cases, the intensity of non-doped Ge column is much higher than Si. Hence, the visibility of the dopant atom is lower in higher Z crystal.

As previously discussed, visibility of a dopant atom is higher at certain positions. These positions are expected to change with the host material, even with exactly same crystal structure

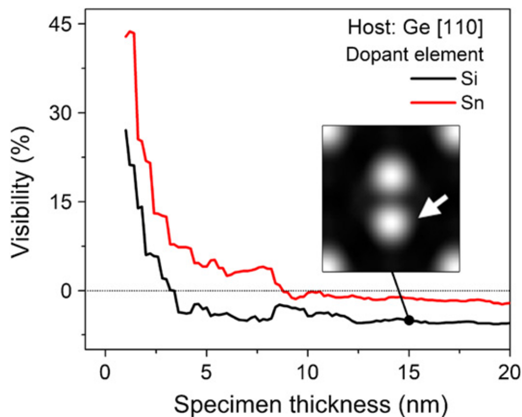

Fig. 8. Visibility of dopant Si and Sn dopant atoms in ADF-STEM images located 0.8 nm from the entrance surface in Ge [1 1 0] as a function of specimen thickness. The 100 keV aberration-corrected probe was used in these simulations. The arrow in ADF-STEM image points to the atomic column where Si dopant atom is located in 15 nm thick Ge host.

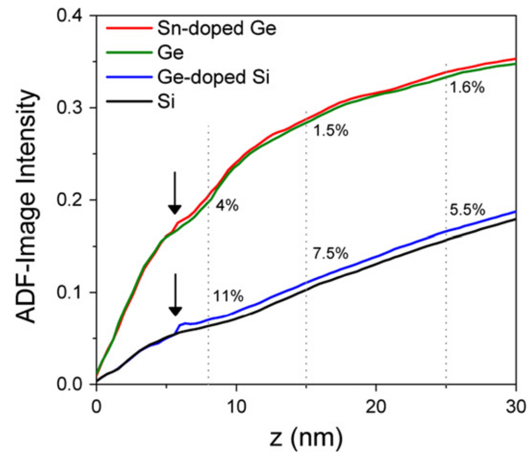

Fig. 10. ADF image intensity of atomic columns as a function of specimen thickness for Si and Ge crystals oriented along [1 1 0] direction with and without single dopant atom inside. Si was doped with Ge, and Ge doped with Sn, $\Delta Z=18$. Position of the dopant atom (at depth $d=5.7$ nm) is indicated with arrow. The dopant atom visibility for different thicknesses of the host is also indicated. The 100 keV aberration-corrected probe was used in these simulations.

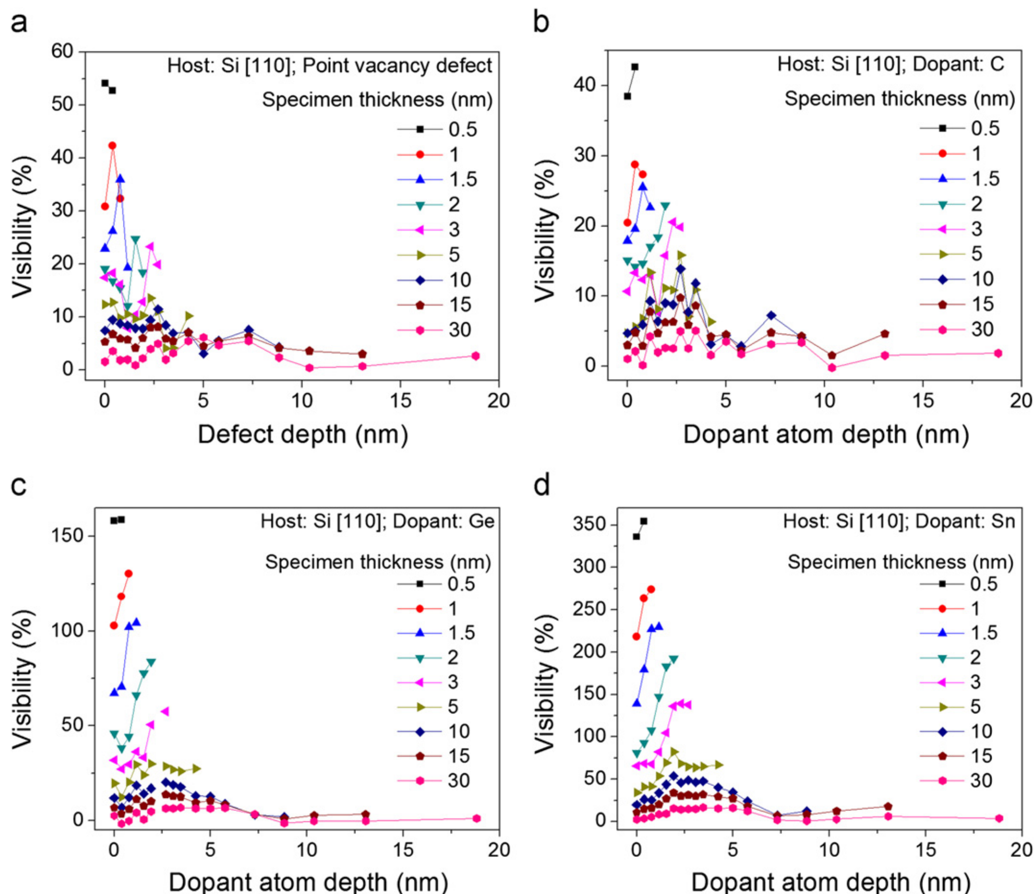

Fig. 9. Visibility of point vacancy (a), and substitutional C (b), Ge (c), and Sn (d) atoms in Si [1 1 0] as a function of depth. 100 keV aberration-corrected probe was used in these simulations.

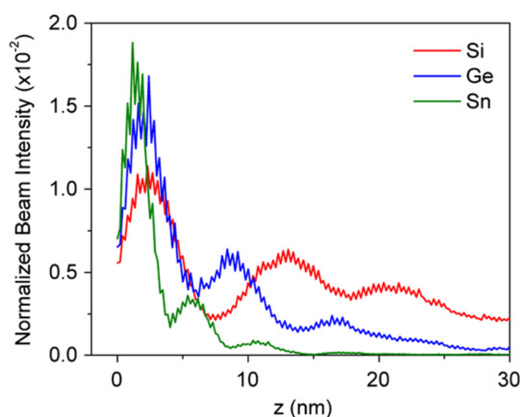

Fig. 11. Incident beam intensity as electrons of the probe, located on an atomic column, propagate along [1 1 0] crystallographic orientations in Si, Ge and Sn. The 100 keV aberration-corrected probe was used in these simulations.

and similar lattice constant, since beam intensity profiles are different for different host materials. Simulated beam intensity profiles as it propagates through an atomic column in [1 1 0] Si, Ge and Sn are presented in Fig. 11. The period of oscillations visibly decreases with increasing atomic number of the crystal from 10 nm in Si to 6.5 nm in Ge to 4 nm in Sn. Additionally, the loss of beam intensity occurs at lower depths for higher Z hosts. These observations are in agreement with Hillyard et al. [37,38] who also report that a channelled probe travels less distance in heavier elements. This suggests that the range of depth for detecting a dopant atom is smaller in hosts with heavier elements when it is aligned along zone axis, i.e. strong channelling conditions.

3.6. Effect of probe size and voltage

The effects of different probe parameters on visibility of a dopant atom are examined to identify conditions that can potentially improve the visibility. We compared the visibility of Sn dopant atom inside crystalline Si host for four STEM probes: 100 keV aberration-corrected (with probe size of 0.8 Å) and non-corrected (1.7 Å), and 300 keV aberration-corrected (0.5 Å) and non-corrected (1.7 Å), see Fig. 2. Here Si was imaged in the [1 1 0] orientation. Fig. 12(a) shows that when Sn is located on the entrance surface both 100 and 300 keV non-corrected probes make the dopant atom almost equally visible in a ADF images. For aberration-corrected probes 300 keV acceleration voltage with smaller probe size leads to a slightly higher visibility than 100 keV. These simulations indicate that increasing the energy of incident electrons does not necessarily improve detection of single dopant atoms and, therefore, beam energy should rather be optimized to minimize sample damage. However, probe size does improve detection.

Beam propagation is significantly different for different probes in both, magnitude of intensity and positions of maxima, see Fig. 12(b). Aberration-corrected probes have their first intense peak at very low depths <5 nm, where the non-corrected beams peak at depths 8–15 nm. The period between consecutive peaks in the channelling beam for aberration-corrected probes is <10 nm, significantly less than the period of non-corrected probes, which is about 20–25 nm. These differences are primarily due to wider convergence angle and shorter depth of focus in aberration-corrected probes. The similarities between the two aberration-corrected and the two non-corrected probes are the reasons why the visibility of dopant atom in ADF-STEM images is similar for each probe pair.

Since the dependence of visibility on dopant atom position follows the beam intensity profile inside a sample, the peak

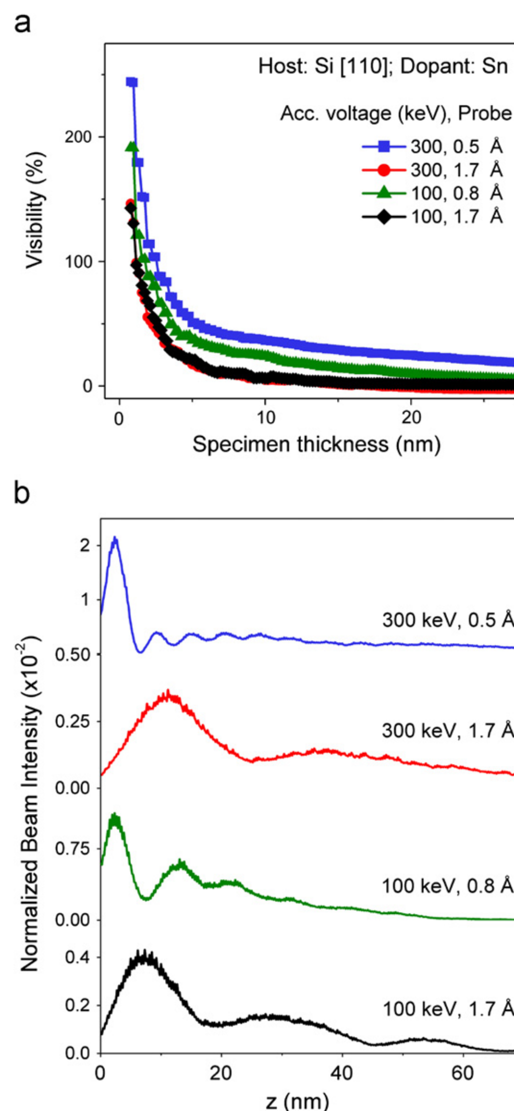

Fig. 12. (a) Visibility of Sn dopant atom in ADF-STEM images in Si [1 1 0] calculated using 100 and 300 keV electron beams with and without aberration-correction. Sn is located on the entrance surface. (b) Beam intensity profiles in Si along [1 1 0] direction as a function of propagation depth.

visibility positions of dopant atom are different for different probes. If a dopant atom is located at 4–5 nm below beam entry surface, an aberration-corrected probe will clearly have an advantage. However, an aberration-corrected probe should not always be the probe of choice for detection of single dopant atom inside the sample. For instance, a dopant atom located 10 nm from the entrance surface has about 6% higher visibility when imaged using non-corrected 1.7 Å probe instead of aberration-corrected 0.8 Å probe, as shown in Fig. 13. Hence, in some cases non-corrected probe can be more useful for identifying the presence of a dopant atom than aberration-corrected probe, consistent with predictions by Dwyer and Etheridge [22]. Examination of the material with both kinds of probes might offer better insight about the position of the dopant with more accuracy than with a single probe.

3.7. Effect of beam source size

For STEM with aberration-corrected probe, the effects of the finite probe size can often be non-negligible. The demagnified

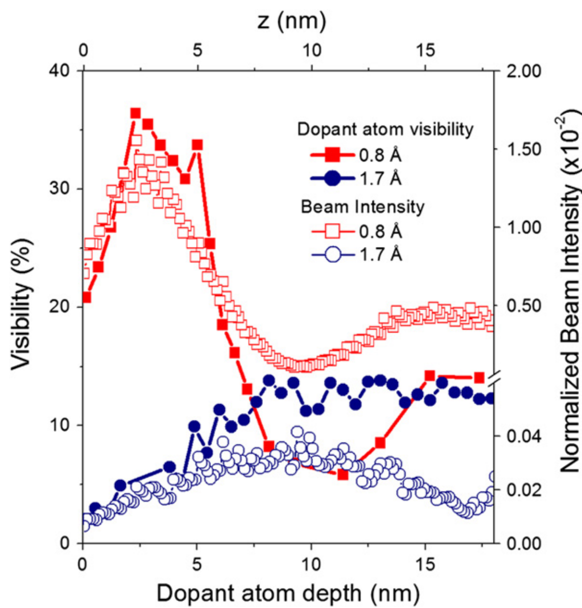

Fig. 13. Visibility of Sn dopant atom in ADF-STEM images in 25 nm thick Si crystal oriented along [1 0 0] direction calculated for different dopant atom positions. For comparison beam intensity profiles in same crystal is also shown. The 100 keV aberration-corrected probe was used in these simulations.

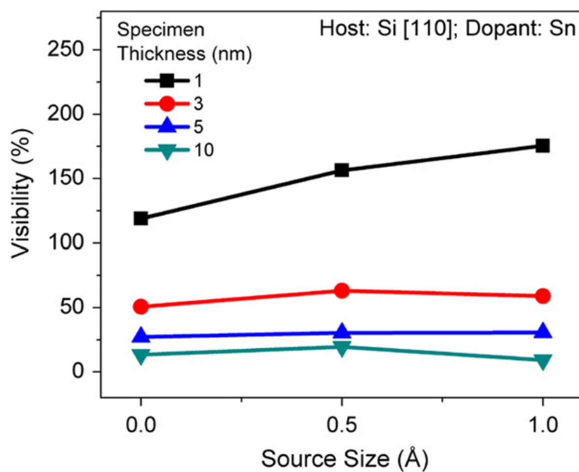

Fig. 14. (a) Visibility of Sn dopant atom in ADF-STEM images in Si [1 1 0] calculated using 0, 0.5 and 1 Å source sizes. Four different specimen thicknesses were considered and in all cases the dopant atom was located at the specimen entrance surface. The 100 keV aberration-corrected probe was used in these simulations.

image of the electron source in the specimen plane, depending on beam current, can be in order of 1 Å [39–41]. This results in additional incoherent broadening of the effective STEM probe function [24]:

$$h_{probe}^{eff}(\vec{x}) = h_{probe}(\vec{x}) \otimes h_{source}(\vec{x}), \quad (3)$$

where $h_{probe}(\vec{x})$ is the STEM probe spread function and $h_{source}(\vec{x})$ is the source function with typical Gaussian distribution. To evaluate the effects of the finite source size on visibility of the dopant atom we simulated the visibility of Sn dopant atom located on Si [1 1 0] entrance surface using a 100 keV aberration-corrected probe for source sizes 0, 0.5 and 1 Å (see Fig. 14). This increase in probe diameter due to finite source size can introduce slight changes in beam channelling pattern resulting in mostly small changes in dopant atom visibility as were observed here.

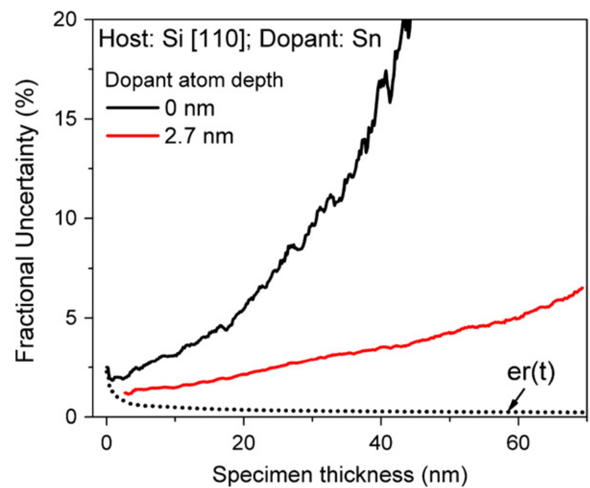

Fig. 15. Fractional uncertainty in visibility of Sn dopant atoms in Si [1 1 0] due to statistical noise in experiment as a function of specimen thickness. er(t) is the standard error in ADF-STEM image intensity as a function of specimen thickness.

3.8. Standard error

While the exact noise level in any ADF-STEM measurement depends on the particular design and the make of the microscope, we can evaluate the standard error (or statistical noise) in the ADF signal and in the visibility of the dopant atoms as a function of specimen thickness, t. Applying the general definition of standard error to ADF-STEM image intensity, I_{adf}, as [42]

$$er(t) = \frac{\delta I_{adf}(t)}{I_{adf}(t)} \times 100\% = \frac{1}{\sqrt{N(t)}} \times 100\%, \quad (4)$$

where the number of electrons scattered to the ADF detector, $N(t)$, can be expressed as

$$N(t) = \frac{I_0}{e}\tau \times f(t). \quad (5)$$

Here I_0 is the beam current irradiating the sample, τ is the dwell time of the scanning probe and $f(t)$ is the fraction of incident beam that scatters into the conical angle of the ADF detector. Calculated standard error in ADF signal of Si [1 1 0] atomic column for 100 keV incident beam as a function of specimen thickness for typical parameters of an aberration-corrected STEM: $I_0 \approx 100$ pA, $\tau \approx 1$ ms [43], is shown in Fig. 15. Multislice simulated $f(t)$ (or normalized ADF intensity) for the 54–200 mrad ADF detector was used here (see Fig. 12). The standard error for the visibility of Sn dopant atom in Si [1 1 0] propagating through Eq. (1) was also evaluated and the results were presented in Fig. 15.

As can be seen from Fig. 15, while the statistical noise can be different for different positions of dopant atom and should be calculated for each specific case, for most practical specimen thicknesses ($\lesssim 40$ nm) a standard error lower than 20% can be expected and in some cases can be even as low as 3%. Such low level of statistical noise suggests that most of the results presented here can be tested experimentally.

4. Discussion

Simulated data on the visibility of a dopant atom as a function of specimen and probe parameters presented systematically in the previous section for practical cases shows, in addition to expected intuitive behavior, also clear non-linearity of trends in visibility. Since the effects of some parameters are coupled, it is difficult to completely separate and provide simple behavioral

trends for every parameter. For example, while expected general $1/t$-type decrease in visibility with increase in specimen thickness, t, was observed in many cases (see Figs. 4 and 8), an Sn dopant atom located at the entrance surface of Si [1 1 0] has visibility below noise level in specimens thicker than 20 nm, whereas Sn dopant atom located 5 nm below the entrance surface is visible (with 10% visibility) even in a 70 nm thick Si [1 1 0] specimens.

The relationship between the position of a dopant atom and its visibility in ADF-STEM image is not simple: several different locations of dopant atom can lead to the same contrast between doped and non-doped atomic columns. For instance, an Sn dopant atom located on the entrance surface in 3 nm thick Si [1 1 0] has 66% visibility. Sn dopant atom, located 2.7 below the entrance surface, in 5 nm thick Si [1 1 0] has also 66% visibility. Moreover, different types of dopant atoms can also have the same calculated visibility. For example, a Ge dopant atom, located 1.2 nm below the entrance surface in a 2 nm thick Si oriented long [1 1 0] direction also has 66% visibility. Thus, determination of dopant atom position requires at least knowledge of dopant identity and specimen thickness, which can be measured using low-loss EELS data [44] or from convergent beam electron diffraction (CBED) patterns [45,41]. However, even with specimen thickness, dopant element, and probe conditions known, two different dopant atom positions can still lead to the same visibility (see Fig. 9).

Essentially, to determine species of a dopant atom or its exact location inside the host crystal, all the factors that affect visibility must be provided. When some of these factors are missing, simulations such as one used here, can be used to estimate the possible ranges. For instance, if an Sn-doped Si [1 1 0] specimen is examined with the 100 keV aberration-corrected probe and the visibility of the dopant atom is 66% (see Fig. 9(d)), the specimen thickness must be in a range from 2 to 10 nm, since $V > 80\%$ at all positions if thickness $t < 2$ nm and, $V < 60\%$ if thickness is $t > 10$ nm.

Another result showing the extent to which intensity of doped columns can be counter-intuitive is the presence of negative values of visibility at certain specimen thicknesses although $Z_{Dopant} > Z_{Host}$ (see Figs. 6(b), 9(c) and 10). For instance, Sn dopant atom at 9 nm depth in 25 nm thick Si [1 1 1] has -4% visibility, see Fig. 9(c). Comparison of beam intensity profiles of doped and pure columns shows that the beam intensity of a doped column is less than the intensity of a pure column at certain specimen thicknesses, as shown in Fig. 16. Atoms exposed to fewer incident electrons will contribute less to ADF image intensity. Hence, a doped column can have lower intensity than the pure host column even though $Z_{Dopant} > Z_{Host}$. Similarly, a doped column can have higher intensity than a pure column when $Z_{Dopant} < Z_{Host}$ (see Fig. 8).

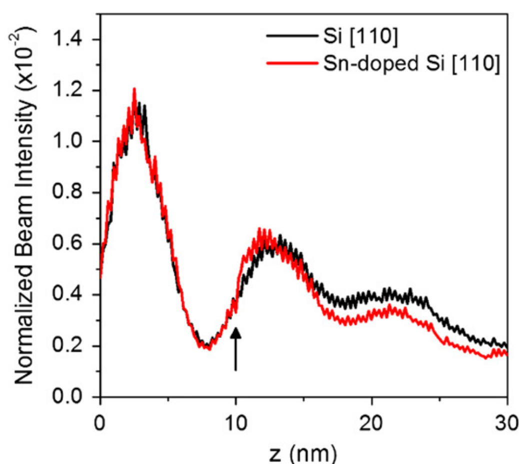

Fig. 16. Incident beam intensity as electrons of the probe, located on the atomic column, propagate along [1 1 0] crystallographic orientations in Si host with and without Sn dopant atom. Position of the dopant atom is indicated with an arrow ($d = 10$ nm). 100 keV aberration-corrected probe was used in these simulations.

Despite all the complications, some intuitive trends are also observed. Visibility of dopant atoms in high-Z hosts is relatively low. For example, in Ge with $Z = 32$, unlike in Si samples, dopant atom is detectable only in a few nm thick specimens. Therefore, if there is a choice, specimens with lower atomic number should be used for detection of single dopant atoms inside. Results show that while $\Delta Z = 2$ can be detected in Si and lighter elements, larger ΔZ is required for different hosts, dopant atom positions, and specimen thicknesses. For better visibility of a dopant atom some crystal orientations are more favourable. For example, in Si, [1 0 0] crystal orientation provides considerably higher visibility than [1 1 1] and [1 1 0] orientations for all dopant atom positions. Thus, testing different crystal orientations for different materials may prove beneficial in detecting dopant atoms. For cases when dopant atom is located at the exist surface the visibility can be approximated as $V = A \cdot |Z^n_{Dopant} - Z^n_{Host}|$, where A is normalization constant and n has a value between 1.5 and 2, consistent with modified Rutherford scattering theory [34]. However, when dopant atom is in the bulk of the host crystal, it will change the beam channelling pattern (see Fig. 16) and such simple model can not be used.

Similar to previous reports [11,17] we observed that the visibility of a dopant atom is strongly correlated with the beam intensity profile, see Fig. 13. Visibility is highest at the depths where the beam intensity is the highest. Channelling of the incident beam along the atomic column is different in different crystals. For a given crystal the beam intensity profile also varies with changes in probe parameters, as shown in Fig. 12. Hence, different probes can be used to enhance detection of dopant atom located at different positions. Although resolution is determined by probe size, a smaller probe is not necessarily beneficial in detecting dopant atoms.

The visibility of the dopant atom can also be changed, even enhanced, by changing the defocus value of the probe. Lupini et al. [17] observed that different doped columns are brighter at different defocus values. Changing defocus also changes the beam channelling. The depth at which the probe is focused is not the depth at which the beam has the highest intensity. Hence, the defocus value leading to the highest intensity of a doped column in an ADF-STEM image cannot be used as the depth of the dopant atom. Similar results were observed by Xin et al. [13] studying Sb-doped Si. While tuning the defocus value can be used to enhance the visibility of the dopant atom, it will also degrade the lateral resolution of the microscope, which is not desired. Obtaining through focal series ADF images might be a solution. It should be noted that the chromatic aberrations and probe tails (unique for each experiment) might also influence the visibility of the dopant atom, but the effects are expected to be small, since they are, in most cases, only relatively small corrections to STEM probe function.

5. Conclusion

Results from multislice simulations show that while the doped atomic column can often be identified in high-resolution ADF-STEM images, determination of the dopant atom location inside the column requires comparison with simulated images. The ADF-STEM image intensity of the atomic column with dopant atom is non-intuitively dependent on many factors, such as specimen thickness and crystallographic orientation with respect to the incident beam, dopant atom type and position inside the host, the crystal structure and composition of the host material,

and on properties of the STEM probe. The analysis presented here provides insight to some observed trends and can be used as practical guidelines for understanding which systems allow imaging individual dopant atoms and which do not.

The number of electrons scattered by a dopant atom into the ADF detector depends on the interaction of the incident STEM probe and the specimen. Similarly, the contribution of a dopant atom to inelastic scattering of incident electrons will also depend on probe and the specimen parameters. Hence, a quantitative EELS analysis of the detectability of dopant atom with EELS also has to be based on understanding beam intensity profile, dopant position, and other specimen features examined here.

Acknowledgments

This work was supported partially by the MRSEC Program of the National Science Foundation under Award Number DMR-0819885 and the Abu Dhabi-Minnesota Institute for Research Excellence (ADMIRE); a partnership between the Petroleum Institute of Abu Dhabi and the Department of Chemical Engineering and Materials Science of the University of Minnesota. We acknowledge receiving technical help from Dr. Ravi Chityala and access to computational resources from University of Minnesota Supercomputing Institute.

References

[1] J.C. Meyer, C.O. Girit, M.F. Crommie, A. Zettl, Nature 454 (2008) 319.
[2] A.V. Crewe, J. Wall, J. Langmore, Science 168 (1970) 1338.
[3] M. Haider, G. Braunshausen, E. Schwan, Optik 99 (1995) 167.
[4] O.L. Krivanek, N. Dellby, A.J. Spence, R.A. Camps, L.M. Brown, in: J.M. Rodenburg (Ed.), Institute of Physics Conference Series (EMAG Meeting Proceedings), vol. 153, 1997, p. 35.
[5] M. Haider, H. Rose, S. Uhlemann, B. Kabius, K. Urban, J. Electron. Microsc. 47 (1998) 395.
[6] O.L. Krivanek, N. Dellby, A.R. Lupini, Ultramicroscopy 78 (1999) 1.
[7] P.E. Batson, O.L. Krivanek, N. Dellby, Nature 418 (2002) 617.
[8] P.D. Nellist, M.F. Chisholm, N. Dellby, O.L. Krivanek, M.F. Murffit, Z.S. Szilagyi, A.R. Lupini, A. Borisevich, W.H. Sides, S.J. Pennycook, Science 305 (2004) 1741.
[9] K.A. Mkhoyan, P.E. Batson, J. Cha, W.J. Schaff, J. Silcox, Science 312 (2006) 1354.
[10] J. Fertig, H. Rose, Optik 59 (1981) 407.
[11] R.F. Loane, E.J. Kirkland, J. Silcox, Acta. Crystallogr. A 44 (1988) 912.
[12] P.M. Voyles, D.A. Muller, E.J. Kirkland, Microsc. Microanal. 10 (2004) 291.
[13] H.L. Xin, V. Intaraprasonk, D.A. Muller, Appl. Phys. Lett. 92 (2008) 013125.
[14] P.M. Voyles, D.A. Muller, J.L. Grazul, P.H. Citrin, H.J.L. Gossmann, Nature 416 (2002) 826.
[15] M. Varela, S.D. Findlay, A.R. Lupini, H.M. Christen, A.Y. Borisevich, N. Dellby, O.L. Krivanek, P.D. Nellist, M.P. Oxley, L.J. Allen, S.J. Pennycook, Phys. Rev. Lett. 92 (2004) 095502.
[16] N. Shibata, S.D. Findlay, S. Azuma, T. Mizoguchi, T. Yamamoto, Y. Ikuhara, Nat. Mater. 8 (2009) 654.
[17] A.R. Lupini, A.Y. Borisevich, J.C. Idrobo, H.M. Christen, M. Beigalski, S.J. Pennycook, Microsc. Microanal. 15 (2009) 441.
[18] Y. Sato, T. Mizoguchi, N. Shibata, T. Yamamoto, T. Hirayama, Y. Ikuhara, Phys. Rev. B 80 (2009) 094114.
[19] H. Okuno, J.-L. Rouvi Aïe, P.-H. Jouneau, P. Bayle-Guillemaud, B. Daudin, Appl. Phys. Lett. 96 (2010) 251908.
[20] R.R. Vanfleet, M. Robertson, M. McKay, J. Silcox, in: AIP Conference Proceedings, vol. 449, 1998, p. 901.
[21] R.F. Loane, P. Xu, J. Silcox, Acta. Crystallogr. A 47 (1991) 267.
[22] C. Dwyer, J. Etheridge, Ultramicroscopy 96 (2003) 343.
[23] J.M. Cowley, A.F. Moodie, Acta. Crystallogr. 10 (1957) 609.
[24] E.J. Kirkland, Advanced Computing in Electron Microscopy, second ed., Springer, 2010.
[25] Alternating (111) planes of atoms in Si are spaced apart at 0.8 and 2.35 Å. Due to the unequal spacing, Si (111) cannot be sliced so that each slice contains exactly one plane of atoms. Therefore, STEM images with two slice thicknesses, 0.7 and 1 Å, were simulated. Results show that both slice thicknesses lead to the same intensity around each atomic column. Consequently, results are not sensitive to this small range of slice thicknesses, and 0.7 Å slice thickness is used in Si (111) simulations.
[26] K.A. Mkhoyan, S.E. Maccagnano-Zacher, E.J. Kirkland, J. Silcox, Ultramicroscopy 108 (2008) 791.
[27] J.S. Reid, J.D. Pirie, Acta. Crystallogr. A 36 (1980) 957.
[28] V.F. Sears, S.A. Shelley, Acta. Crystallogr. A 47 (1991) 441.
[29] P.M. Voyles, J.L. Grazul, D.A. Muller, Ultramicroscopy 96 (2003) 251.
[30] S.E. Maccagnano-Zacher, K.A. Mkhoyan, E.J. Kirkland, J. Silcox, Ultramicroscopy 108 (2008) 718.
[31] To calculate the error in visibility values, Si [1 0 0] Sn-doped specimen was imaged over a 7×7 Å^2 area using a 100 keV aberration-corrected probe, averaged over 10 phonon configurations. This simulation was repeated nine times. The mean standard deviation between each set of 9 pixels was used as uncertainty for the intensity of an atomic column. Propagation of error calculation for the Eq. (1) led to less then 7% fractional uncertainty in visibility. Increasing the number of phonon configurations can further improve the accuracy in simulated results. Uncertainty due to experimental noise depends on the experimental setting and is not considered here.
[32] H.L. Xin, D.A. Muller, J. Electron. Microsc. 58 (2009) 157.
[33] A.Y. Borisevich, A.R. Lupini, S.J. Pennycook, Proc. Natl. Acad. Sci. 103 (2006) 3044.
[34] E.J. Kirkland, R.F. Loane, J. Silcox, Ultramicroscopy 23 (1987) 77.
[35] S.J. Pennycook, L.A. Boatner, Nature 336 (1988) 565.
[36] S.J. Pennycook, Ultramicroscopy 30 (1989) 58.
[37] S. Hillyard, R.F. Loane, J. Silcox, Ultramicroscopy 49 (1993) 14.
[38] S. Hillyard, J. Silcox, Mater. Res. Soc. Symp. Proc. 332 (1994) 361.
[39] S. Hillyard, J. Silcox, Ultramicroscopy 52 (1993) 325.
[40] J.M. LeBeau, S.D. Findlay, L.J. Allen, S. Stemmer, Phys. Rev. Lett. 100 (2008) 206101.
[41] J.M. LeBeau, S.D. Findlay, X. Wang, A.J. Jacobson, L.J. Allen, S. Stemmer, Phys. Rev. B 79 (2009) 214110.
[42] J.R. Taylor, An Introduction to Error Analysis, second ed., University Science Books, 1997.
[43] O.L. Krivanek, N. Dellby, M.F. Murfitt, M.F. Chisholm, T.J. Pennycook, K. Suenaga, V. Nicolosi, Ultramicroscopy 110 (2010) 935.
[44] R.F. Egerton, Electron Energy Loss Spectroscopy in the Electron Microscope, second ed., Plenum, 1996.
[45] P.M. Kelly, A. Jostons, R.G. Blake, J.G. Napier, Phys. Status Solidi A 31 (1975) 771.